

Subsurface Fluid Injection and Energy Storage

Q. Li, M. Kühn (Guest editors)

REGULAR ARTICLE

OPEN ACCESS

Fault slippage and its permeability evolution during supercritical CO₂ fracturing in layered formation

Xiaochen Wei^{1,2,3}, Jingxuan Zhang¹, Qi Li^{2,4,*}, Xiangjun Liu³, Lixi Liang³, and Lili Ran¹

¹School of Geoscience and Technology, Southwest Petroleum University, 610500 Chengdu, PR China

²State Key Laboratory of Geomechanics and Geotechnical Engineering, Institute of Rock and Soil Mechanics, Chinese Academy of Sciences, 430071 Wuhan, PR China

³State Key Laboratory of Oil and Gas Reservoir Geology and Exploitation, Southwest Petroleum University, 610500 Chengdu, PR China

⁴University of Chinese Academy of Sciences, 100049 Beijing, PR China

Received: 17 April 2019 / Accepted: 18 September 2019

Abstract. Understanding the hydromechanical responses of faults during supercritical CO₂ fracturing is important for reservoir management and the design of energy extraction systems. As small faults are widespread in Chang 7 member of the *Yanchang Formation*, Ordos Basin, China, supercritical CO₂ fracturing operation has the potential to reactive these undetected small faults and leads to unfavorable fracking fluid migrate. In this work, we examined the role of fault slippage and permeability evolution along a small fault connecting the pay zone and the confining formation during the whole process of fracturing and production. A coupled hydromechanical model conceptualized from actual engineering results was introduced to address the main concerns of this work, including, (1) whether the existence of a undetected small fault would effectively constrain the hydraulic fracture height evolution, (2) what the magnitude of the induced microseismic events would be and (3) whether the permeability change along the fault plane would affect the vertical conductivity of the confining formation and thus increase the risk for the fracturing fluid to leak. Our results have shown that the initial hydrofracture formed at the perforation and propagated upward, once it merged with the fault surface, the existence of an undetected small fault would effectively constrain the hydraulic fracture height evolution. As fracturing continued, further slippage spread from the permeability increase zone of high permeability to shallower levels, and the extent of this zone was dependent on the magnitude of the fault slippage. At the end of extraction, the slip velocity decreases gradually to zero and the fault slippage finally reaches stabilization. In general, undetected small faults in targeted reservoir may not be the source of large earthquakes. The induced microseismic events could be considered as the sources of acoustic emission events detected while monitoring the fracturing fluid front. Due to the limited fault slippage and lower initial permeability, the CO₂ fracturing operation near undetected small faults could not conduct preferential pathway for upward CO₂ leakage or contaminate overlying shallower potable aquifers.

1 Introduction

The stimulation of hydraulic fractures as a technique used to enhance hydrocarbon recovery from low-permeability reservoirs involves pumping fracturing fluids (water, particles and additives) into vertical or horizontal wells drilled through the formation (Montgomery and Smith, 2010; Swartz, 2011). The fracturing fluids pumped through the well create fractures when the fluid pressure exceeds the tensile strength and the least principal stress of the rock being fractured (Hubbert and Willis, 1957), and the

fractures propagate until the stress intensity at the fracture tip decreases below the critical stress intensity of the fracturing formation (Savalli and Engelder, 2005). Faults are planar fractures or discontinuities in geological formations that can have a significant impact on the hydraulic fracturing operation (Childs *et al.*, 1996). In many cases, the fault zone displays a damage zone including secondary fault cores embedded in a severely fractured zone (Jeanne *et al.*, 2014). Faults and fractures could significantly affect the hydraulic fracturing process, once the upward-propagating hydraulic fractures connect with a typical fault, the impermeable fault core acts as a partial flow barrier while the high-permeability fractured zone acts as a conduit through the formation (Figueiredo *et al.*, 2015), which could heighten the possible

* Corresponding author: qli@whrsm.ac.cn

environmental and human health implications associated with the subsurface migration of fracturing fluid and brine (Vengosh *et al.*, 2014). While it is common sense to keep away from known major faults to avoid seismic hazards generated by hydraulic fracturing (Abercrombie, 1995; Kanamori and Anderson, 1975), the potential hydromechanical responses of undetected faults (*i.e.*, faults that were not identified at the screening stage of the project) to hydraulic fractures and the influence on the vertical conductivity of the overlying aquifers have not been thoroughly studied. The fracturing process involves forced supercritical CO₂ injection into hydrocarbon reservoirs and has the potential to reactivate the undetected small faults, the analysis of low-magnitude microseismic events induced by fault slippage during the fracturing process gives insights into the fracturing fluid front and the effective stimulated reservoir volume (Ishida *et al.*, 2012; Roche and van der Baan, 2015).

A considerable number of numerical investigations have been carried out trying to understand the responses of hydraulic fracture-fault interactions (Figueiredo *et al.*, 2017; Rutqvist *et al.*, 2013; Zoback *et al.*, 2012). The research works studied can be categorized into two main groups (Khoei *et al.*, 2016): the first category is concerned with the mechanical interaction between hydraulic fracturing and natural faults. Dong and Pater (2001) improved the usual displacement discontinuity method to describe straight-line and curved cracks, and the fault was found to have a significant effect on crack reorientation. Akulich and Zvyagin (2008) investigated the interaction between a pre-existing natural fault and a hydraulic fracture propagating in an infinite impermeable elastic medium, and the modeling results indicated that the hydraulic fracture-fault interaction is highly dependent on the fluid viscosity. Dyskin and Caballero (2009) investigated a tensile crack approaching a sliding interface without resistance to opening with a finite element method, and computer simulations showed that a frictionless interface produces a concentration of stress at the ends of the interface where no fault slippage takes place. Dahi-Taleghani and Olson (2011) presented a complex hydraulic fracturing analysis by using an extended finite element model to optimize the operation parameters; they concluded that hydraulic fracture propagation could exert both tensile and shear stresses on natural fractures at the fracture intersections. Rutqvist *et al.* (2013) assessed the potential for notable seismic events triggered by shale-gas hydraulic fracturing operations, and the modeling simulations indicated that the presence of faults increases the magnitude of microseismic events due to the larger surface area available for rupture. Khoei *et al.* (2016) adopted an enriched extended finite element method to expose the mechanism of interaction between the hydraulic fracture and a pre-existing natural fault considering several conditions, including the varying levels of friction and fault angles, but the fault was described by a simple discontinuity without fault gouge, and the hydromechanical behavior within the fault was not discussed. Based on the degradation of material properties, Figueiredo *et al.* (2017) studied the influence of pre-existing faults on the vertical propagation of a hydrofracture with an elastic-brittle model, and the

fracture propagation was found to decrease with the shear failure of the fault.

The second category is focused mainly on the propagation of hydraulic fracturing when the fracture tip approaches the material interfaces in layered formations or interlayers. In early studies, the capability of material interfaces to contain or deflect fractures was usually analyzed by comparing the ratio of the energy release rates or material toughness (He and Hutchinson, 1989), and stress contrasts were regarded as the predominant influence on hydraulic fracture containment (Warpinski *et al.*, 1982), while material contrasts did not directly control fracture height (Smith *et al.*, 2001). Cleary described a general-purpose numerical scheme to analyze the conditions and possibilities for fractional interfacial slippage leading to interface separation (Cleary, 1978). Jia (2000) studied interface debonding when a crack normally approaches a perfectly elastic-plastic interface and concluded that the interface toughness is the most significant factor in interface debonding. Brenner and Gudmundsson (2004) highlighted that the overpressure within the fracture together with the mechanical properties of the host rock controls the growth of the fracture. Zhou *et al.* (2008) concluded that the fracture might escape from the interface under specific conditions and that the change in the fracture propagation direction would result in various fracture and fluid flow patterns.

Above all, introducing a mechanistic model that promotes the understanding of fault slippage and permeability evolution is a key step to bridge both reservoir characterization and risk management. The main emphases of this work are (1) whether the existence of an undetected small fault would effectively constrain the hydraulic fracture height evolution, (2) what the magnitude of the induced microseismic events would be and (3) whether the permeability change would affect the vertical conductivity of the confining formation and thus increase the risk for the fracturing fluid to leak. To address these questions, we first introduce a numerical model conceptualized from actual engineering results and evaluate the hydrofracture fracture propagation. Then, considering the fracturing fluid diversion into the fault gouge, we investigate the hydromechanical response, including fault slippage and permeability evolution during the whole process of hydraulic fracturing and production. Finally, the roles of the fracturing fluid flow rate, initial fault permeability and fault stiffness in the reference model are separately explored by parametric analyses.

2 Numerical approach

The oil and gas resources of the *Yanchang Formation* of the Mesozoic in the Ordos Basin have great potential for development. In this work, we focus on Fuxian area that locates in the central area of the oil and gas system in the Ordos Basin (Fig. 1a). As shown by the logging data and lithological profile of one well within the study zone (Fig. 1b), reservoirs of thin sand and mudstone interbedding were developed in Chang 7 member of the *Yanchang Formation*.

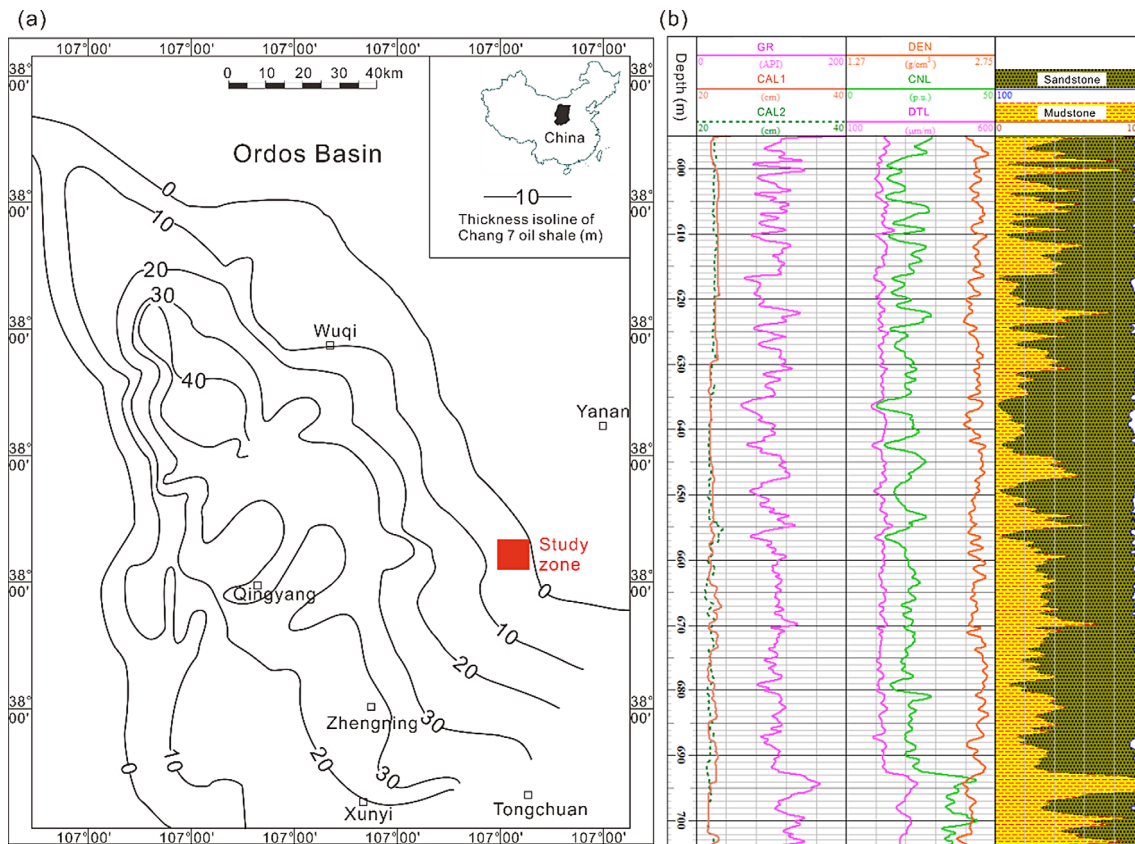


Fig. 1. (a) Location of the study zone and the thickness of isoline of Chang 7 oil shale in Ordos Basin and (b) the logging data and lithological profile of one well within the study zone.

During reservoir stimulation with supercritical CO_2 , once the hydrofracture connects with a small natural fault, the fracturing operation has the potential to reactive the fault and leads to unfavorable fracking fluid migrate.

To study in detail the mechanical and hydraulic response of a natural fault to the reservoir stimulation in the thin sand and mudstone interbedding, we choose a small-scale perforation interval in a horizontal fracturing well from the study zone in Figure 1. As shown in Figure 2a, three geological structural features are generated, and the overlying confining formation is composed of mudstone at depths from 1000.0 m to 1005.0 m, while the pay zone is composed of conglomerate at depths from 1005.0 m to 1007.5 m with an internal horizontal fracturing well. The vertical hydraulic fracturing is initiated by fracking fluid injection into the pay zone at the perforation. By considering the model as vertically symmetrical, the conceptual model of $15 \text{ m} \times 7.5 \text{ m}$ shown in Figure 2b is generalized from the geologic structural features. The small fault zone, with a dip angle of 60° , a length of 4.6 m and width of 0.3 m, is assumed to penetrate the two layers with its centroid located on the stratigraphic boundary. The mesh consists of 81 472 nodes and 80 243 elements, and the elements are more refined near the fracture and the fault.

The Vertical Stress (S_v) component is provided by the weight of the overburden and at 1000 m depth below the surface is 26 MPa. The geostress inversion results show that

the regional stress field is normal fault, and the horizontal stresses do not show significant tendency to change from layer to layer near 1000 m. Thus, for simplification the magnitude of the Horizontal Stress (S_h) component is given by the lateral pressure coefficient $S_h/S_v = 0.6$. As the model is considered saturated, the initial pore pressure is set to linear with a gradient of 10 MPa/km. This condition results in a pore pressure of 10 MPa at the top of our model (-1000 m). Supercritical CO_2 is defined with density of 1.1 g/cm^3 and viscosity of 0.02 MPa s , as the temperature and pressure fall into the critical condition for supercritical CO_2 , it is reasonable to neglect the phase change in this work (Ilieva *et al.*, 2016). The displacements of the left/right boundaries and the bottom are fixed to the normal directions, and the friction coefficient between the fault and the surrounding formation is set to 0.6. In this work, the rock properties are supported by logging data from a practical engineering project. Usually, fault zones are simplified to the formation of a damage zone where the most fractured region appears (Billi *et al.*, 2003), but in this work, the fault zone is subdivided into the fracture zone and the fault core characterized by well-defined planes. The fault zone architecture is shown in Figure 2b, where the properties of the fault fracture zone are influenced by the hydromechanical properties of the surrounding rock. The Young's modulus of the fault is reduced by a factor of 1.5 relative to that of the conglomerate, while the permeability increases five times. In the low-porosity

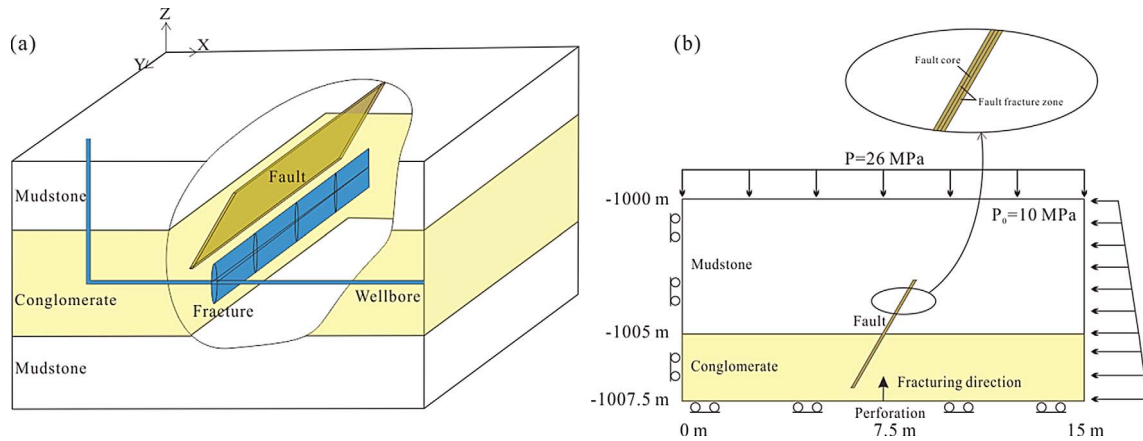


Fig. 2. (a) The generalized geologic structural features and (b) the initial/boundary conditions.

mudstone layer, the Young's modulus is reduced by a factor of 5, and the permeability is increased by 10 times with respect to the mudstone layer (Jeanne *et al.*, 2014). The fault core embedded in the fracture zone is represented by constant hydromechanical properties with $E = 2$ GPa and $K = 10^{-17}$ m²; thus, the fault acts as both a conduit through the caprock and a partial flow barrier within the reservoir (Fig. 3).

We introduce a linear elastic traction-separation law, including a damage initiation criterion and a damage evolution law (Othmani *et al.*, 2011), to define the degradation and eventual failure of a mixed-mode fracture in layered formations. A Mohr-Coulomb constitutive model is adopted to describe the interaction of the fracture propagation and the fault. To simulate the whole process of hydraulic fracture and production, the analysis consists of four steps. In the geostatic step, in order to eliminate the displacement generated by gravity and the initial conditions, the internal forces at the centroid of each element are specified as the initial stress condition. In the subsequent "Pump" step, a Newtonian fluid is injected from the horizontal fracturing well, which is located at the center of the bottom of the model for 80 min. An initial injection rate per unit volume of 4 m³/min is applied. The fracture is described by an embedded cohesive zone without initial separation along the entire fracture path, and the fracturing fluid injection drives the initiation and hydraulic extension of the fracture. Following the "Pump" step, the "Hold" step is conducted to analyze the closing in process for five days. The fluid injection is terminated, and the previously built-up pore pressure in the fracture is allowed to spread into the surrounding formation. An additional zero-velocity boundary condition is applied to the fracture surface to simulate the effect of the proppant material within the fracture. In the final "Extraction" step, an extraction rate per unit volume of 0.4 m³/min is applied to the fracture opening for 30 days to simulate exploitation.

In fractured rock masses, effective stresses (which include the effect of fluid pore pressure) induce changes in hydraulic properties such as permeability and porosity, and the initial values of porosity and permeability are

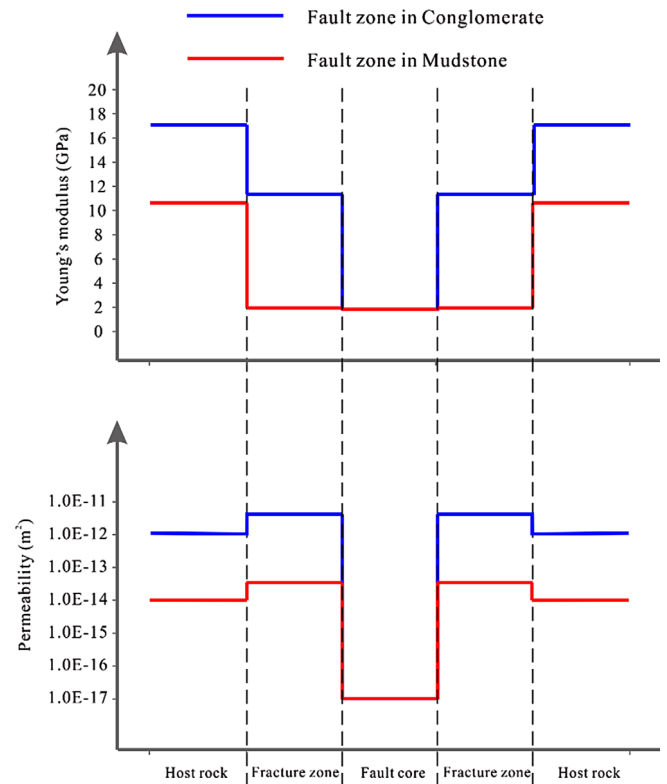


Fig. 3. Hydromechanical properties of a discontinuous damage zone.

corrected by taking into account changes in volumetric strains (Rinaldi *et al.*, 2014). The elastic part of the volumetric behavior of porous materials is modeled accurately by assuming that the elastic part of the change in volume of the material is proportional to the logarithm of the pressure stress:

$$\frac{K}{(1 + e_0)} \ln \left(\frac{p_0 + p_t^{\text{el}}}{p + p_t^{\text{el}}} \right) = J^{\text{el}} - 1, \quad (1)$$

where K is the logarithmic bulk modulus, e_0 is the initial void ratio, p is the equivalent pressure stress defined by $p = -(\sigma_{11} + \sigma_{22} + \sigma_{33})/3$, p_0 is the initial value of the equivalent pressure stress, J^{el} is the elastic part of the volume ratio between the current and reference configurations and p_t^{el} is the elastic tensile strength of the material.

The constitutive behavior for pore fluid flow is governed either by Darcy's law or by Forchheimer's law. Darcy's law is generally applicable to low fluid flow velocities, whereas Forchheimer's law is commonly used for situations involving higher flow velocities. Darcy's law can be thought of as a linearized version of Forchheimer's law. Darcy's law states that under uniform conditions, the volumetric flow rate of the wetting liquid through a unit area of the medium, snV_w , is proportional to the negative of the gradient of the piezometric head (Chapelle *et al.*, 1999):

$$snV_w = -k \frac{\partial \varphi}{\partial x}, \quad (2)$$

where k is the permeability of the medium and φ is the piezometric head, V_w is the wetting liquid is that flow through the volume, defined as (Thomas and Kitanidis, 1989):

$$\varphi \stackrel{\text{def}}{=} z + \frac{u_w}{g\rho_w}, \quad (3)$$

where z is the elevation above some datum and g is the magnitude of the gravitational acceleration, which acts in the direction opposite to z . On the other hand, Forchheimer's law states that the negative of the gradient of the piezometric head is related to a quadratic function of the volumetric flow rate of the wetting liquid through a unit area of the medium (Fiori *et al.*, 1998):

$$snV_w(1 + \beta\sqrt{v_w v_w}) = -k \frac{\partial \varphi}{\partial x}, \quad (4)$$

where β is a velocity coefficient. This nonlinear permeability can be defined to be dependent on the void ratio of the material in equation (5), where u_i and k_i is the void ratio and permeability in the former i step, and n is the constant term (Bloch and Helmold, 1995). As the fluid velocity tends to zero, Forchheimer's law approaches Darcy's law. Additionally, if $\beta = 0$, the two flow laws are identical:

$$k_{i+1} = \left(\frac{u_i}{u_{i+1}} \right)^n k_i. \quad (5)$$

3 Results and parametric analyses

3.1 Mixed mode hydrofracture propagation and pore pressure evaluation

With the mechanical characteristics and geometry defined above, we use this model to investigate the effect of injection on fault activation and seismicity during hydraulic fracturing; comparative analyses such as fault slip, injection pressure distribution, and magnitudes of seismic events are conducted. The mixed-mode hydrofracture propagation

and the corresponding horizontal stress distribution are shown in Figure 4. The horizontal stress distribution within the rectangular region in the model is shown in Figure 4a, and the width of the hydrofracture is magnified 120 times for clear visualization. The fracture extension is parallel to the maximum principal stress direction, and before the hydrofracture connects with the natural fault at about 2200 s, the horizontal stress induced in front of the hydrofracture tip is tensile. Further fracturing allows the hydrofracture tip to propagate upward and merge with the natural fault, as the tensile stress concentration on the opposite side of the fault plane is insufficient to initiate a new fracture that leading to fracture crossing, the natural fault arrests the fracture propagation and leads to permanent termination of the fracture at the fault plane. Afterward, as shown in Figure 4b, this tensile stress results in an opening mode on the natural fault in the vicinity of the intersection, and thus, at this stage, the high-permeability fault fracture zone acts as a conduit connecting deep permeable regions. In the subsequent "Hold" stage, the fault surface opening decreases gradually and finally vanishes at the end of the "Extraction" stage.

The pore pressure evolution at the perforation is recorded in Figure 5a, where I, II and III represent the "Pump" stage, the "Hold" stage and the "Extraction" stage, respectively. Pore pressure initially builds at the perforation and only migrates upward as fluid diffusion occurs; following this movement, the pore pressure increases sharply to 17.4 MPa (Fig. 5a) and decreases after the fracture reaches the fault. The rapidly growing pore pressure increase zone with the upward propagation of the hydrofracture in the fracturing stage is shown in Figures 5b–5d; after the hydrofracture tip merges with the natural fault, instead of penetrating the natural fault, the stress distribution results in an opening mode of the fault (Fig. 5b); this effect occurs because the fracture is inclined to the minimum principal stress direction, and after the fracture reaches the fault, the pore pressure near the fracture tip decreases to less than the minimum pressure necessary to continue propagating the fracture. In the "Hold" stage (Fig. 5e), the previously built-up pore fluid near the fracture diffuses into the surrounding formations, the pore pressure near the perforation starts to decrease while the pore pressure increase zone expands with time and reaches a maximum at the end of this stage (5 days), and the pore pressure diffusion is significantly blocked by the property differences between the conglomerate layer and the overlying mudstone. Afterward, the exploitation results in a remarkable pore pressure decrease near the hydrofracture during the final stage; after 30 days of extraction, the pore pressure near the perforation decreases to 10.8 MPa.

As the maximum pore pressure appears in the "Pump" stage, here, we illustrate the pore pressure evolution at different locations along the fault surface during this stage in Figure 6. As shown, after the fracturing starts, the scope of the pore pressure increase zone extends gradually with time, and thus, the pore pressure in the lower portion of the fault fracture zone (in the conglomerate) increases accordingly. However, due to the relatively lower permeability of the mudstone and the longer seepage path for the fracturing

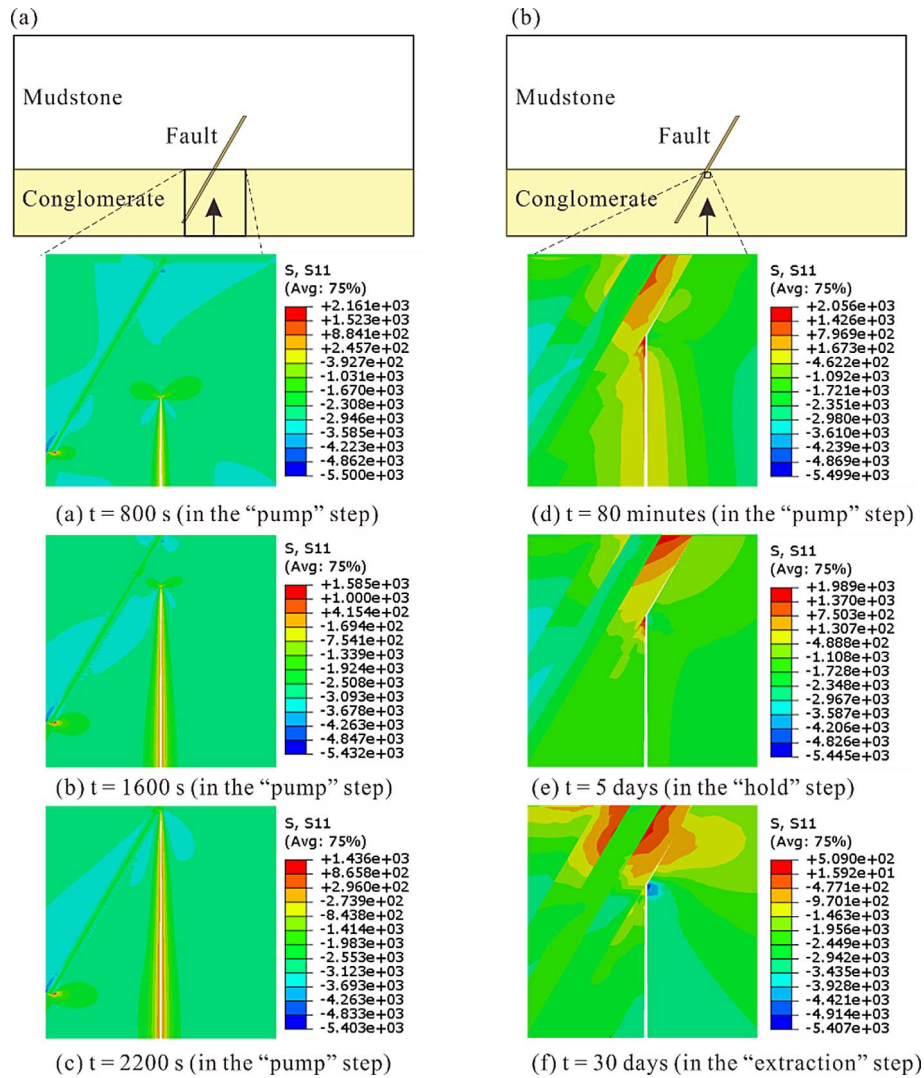


Fig. 4. The mixed-mode hydrofracture propagation and the corresponding horizontal stress distribution at different times.

fluid to reach this layer, the pore pressure in the mudstone is not significantly affected until 2400 s. Then, after the fracture tip merges with the fault plane, the pore pressure along the fracture zone sees a simultaneous increase. At this time, the formerly unaffected pore pressure within the fault fracture zone surrounded by mudstone is enhanced by the flow of fracturing fluid into the fault fracture zone.

3.2 Fault slippage and induced microseismicity

According to the mechanisms of how elevating the pore pressure can bring the fault to slippage illustrated by (Ellsworth, 2013), a fault remains locked as long as the applied shear stress is less than the strength of the contact. During the stimulation injection, the shear stress evolves simultaneously with tensile failure; the activation of the fault is usually initiated by the increase in the shear stress and the decrease in the normal stress that can bring the fault to failure and trigger the nucleation of microseismic events (Wei et al., 2015, 2016). The variations in the

contact stress and shear stress along the fault plane at the ends of the “Pump” stage (green line), the “Hold” stage (blue line) and the “Extraction” stage (black line) are shown in Figure 7. The pore pressure increase at the fault surfaces results in contact stress decrease, and the shear stress increases accordingly within the lower portion of the fault fracture zone in the conglomerate. Then, the pore pressure diffusion increases the magnitude of the stress variation until the end of the “Hold” stage.

In the “Extraction” stage, the extraction effect decreases the magnitude of the stress variation, and reduces the area of the stress change portion on the fault surface. In particular, due to the tensile stress in front of the hydrofracture tip, the opening mode (Fig. 4b) results in a concentration of the contact stress and shear stress in the vicinity of the fault-fracture intersection.

Fault slippage is a key factor in quantitatively evaluating the response of fracture propagation to fault activation (Chong et al., 2017). To illuminate the pattern for the fault to slip, two monitoring points M and N are set, with M

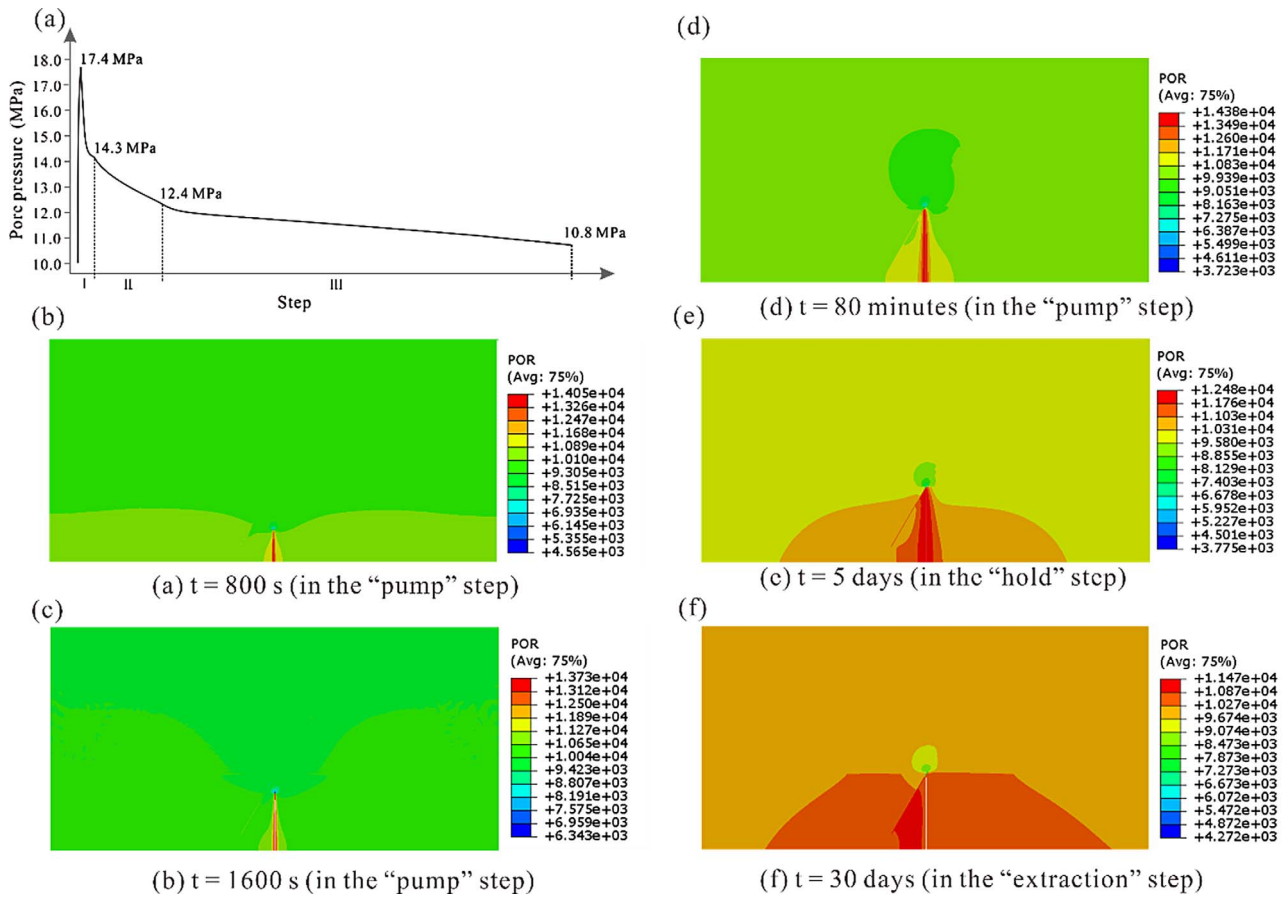


Fig. 5. (a) The pore pressure evolution at the perforation and (b)–(f) the pore pressure increase zone at different times.

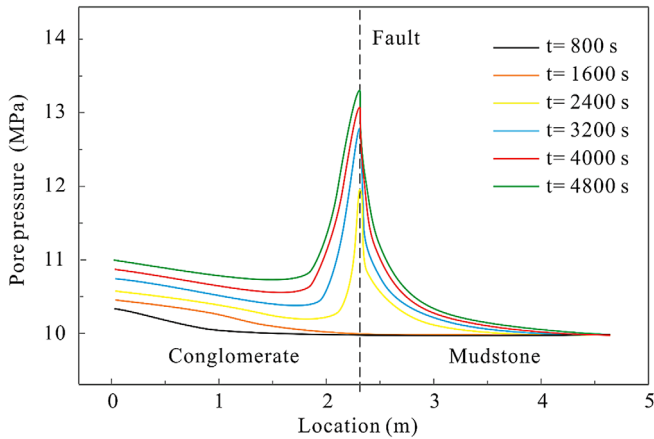


Fig. 6. Pore pressure evolution along the fault surface during the fracturing stage at different times.

located in the middle of the fault portion in the mudstone and N located in the middle of the fault portion in the conglomerate. Figure 8 displays the evolution of the fault slip velocity and slip displacement at monitoring points M and N through the whole Pump–Hold–Extraction process. According to the slippage rate and time, the curves can be split into three stages. Stage I is the rapid slippage

build-up stage; this stage is consistent with the “Pump” step. Since there is a distance of 2.5 m between the perforation and the fault, before the hydrofracture tip merges with the fault zone, the fault stabilization is only affected by the stress perturbation induced by the fracturing operation. When the hydrofracture tip merges with the fault after 2200 s, the pore pressures at the monitoring points change dramatically, and the corresponding induced slippages increase rapidly. The fault mechanical response is sensitive to pore pressure changes, and an increase in pore pressure tends to significantly increase fault slippage during the “Pump” stage in both scenarios; due to the difference in lithological characteristics along the fault, the relatively lower pressure build-up at monitoring point M results in a smaller fault slip velocity and slip displacement than at monitoring point N. After the rapid fault slip stage I, in stage II, which corresponds to the “Hold” stage, the previously built-up pore pressure near the fracture diffuses into the surrounding formations, and the slippage distance decreases with pore pressure dissipation. At this stage, the permeability of the host rock determines the speed at which the trapped fracturing fluid spreads, and the slip rate at monitoring point M is obviously smaller than that in stage I. Stage III is the transition stage of the fault from activation to a stable state; the stress balance is restored, and the slip velocity decreases gradually to zero by the

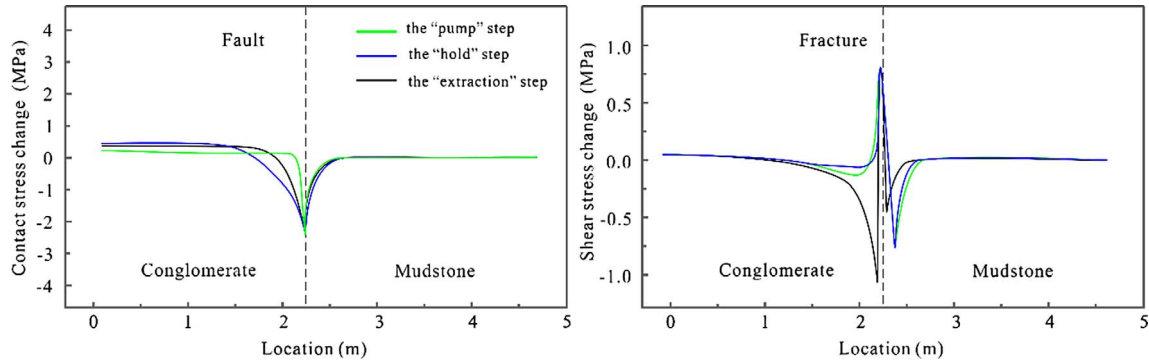


Fig. 7. Variations in contact stress and shear stress along the fault plane at the end of the “Pump” stage (green line), the “Hold” stage (blue line) and the “Extraction” stage (black line).

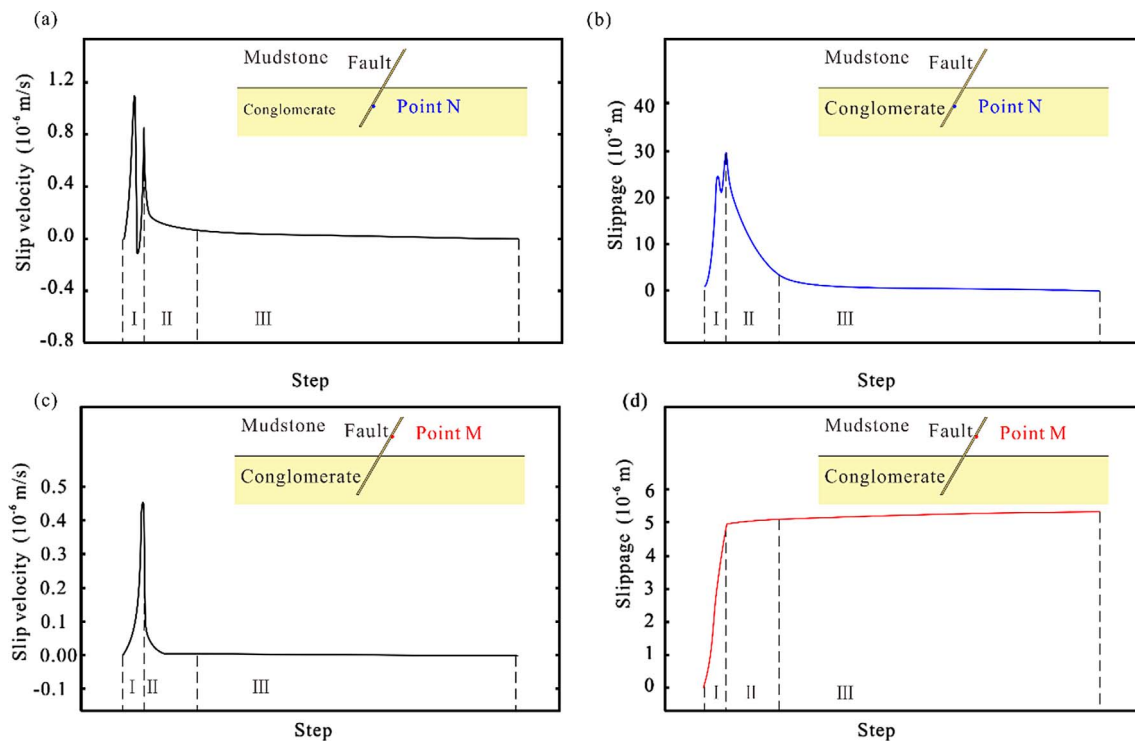


Fig. 8. Evolution of the fault slip velocity and slip displacement at monitoring points M and N through the whole Pump–Hold–Extraction process.

end of extraction; thus, the fault slippage finally reaches stabilization.

In the “Pump” stage, the fault slippage evolution along the fault surface presented in Figure 9a shows similar trend to the pore pressure variation. The maximum slippage is located in the conglomerate before 2200 s and then transfers to the fracture-fault plane intersection after the fracture tip merges with the fault zone. The interplay of the von Mises stress, pore pressure and fault slippage is illustrated in Figure 9b; as shown, the pore pressure change is not the only mechanism for the fault to slip (Davies *et al.*, 2013); the slippage at monitoring point N experiences a two-stage increment. The reservoir rock formation around the fault is in a state of unbalanced stability before fault activation,

and the first stage of fault reactivation is triggered by the stress disturbance caused by hydrofracture propagation and occurs at 1200 s (red line in Fig. 9b). Shortly after the stress dissipation at N, the hydrofracture tip merges with the fault zone, the fracturing fluid can enter the fault, and a fluid pressure pulse can be transmitted to the fault. As a result of poroelasticity, the deformation or “inflation” of the rock due to injection can increase the fluid pressure at monitoring point N (blue line in Fig. 9b). Thus, the maximum fault slippage at N is higher than that at M, where the fault stabilization is only affected by a much lower pore pressure increase (Fig. 6).

Considering layered formations, the magnitude of a seismic event quantified by the scalar seismic moment is

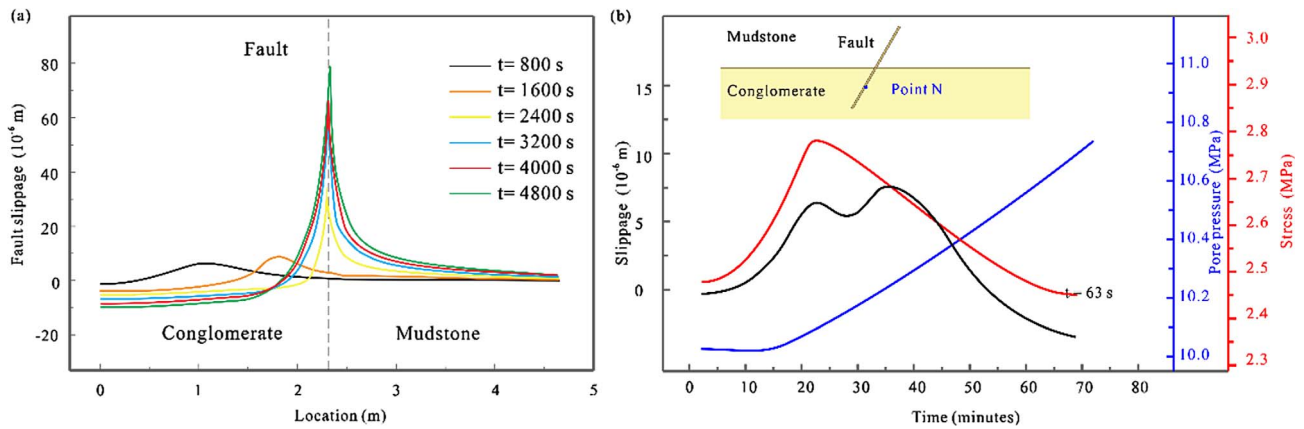


Fig. 9. (a) Fault slippage evolution along the fault surface and (b) the interplay of von Mises stress, pore pressure and fault slippage.

defined as $M_0 = A \times \sum_i^n G_i d_i$, where A is the ruptured area, d_i is the mean slip over the ruptured area, and G_i is the rock shear modulus. The moment magnitude Mw of the fault evolution with time is shown in Figure 10. The simulated moment magnitude of the induced microseismic events generally ranges between $Mw = -1.8$ and -2.6 that could be considered as the sources of acoustic emission events detected while monitoring the fracturing fluid front. The largest events occur within the “Pump” stage when the hydrofracture tip penetrates the conglomerate and merges with the fault surface. Afterward, the microseismicity continues during the “Hold” and “Extraction” stages at decreasing magnitudes.

3.3 Permeability evolution

The permeability evolution of faults is known to be sensitive to dynamic and static stress perturbations as a result of hydraulic fracturing (Mukuhira *et al.*, 2017). Shear dilation together with fault slippage contributes to increases in permeability by breaching the mated contact surface. Here, we record the void ratio change along the fault surface at different times (Fig. 11a) within the “Pump” stage; the void ratio along the fault surface increases with time but decreases at

the end of the “Hold” stage, and continues to decrease until the end of the “Extraction” stage. Because of the limited fault slippage and lower initial permeability, the void ratio change within the upper portion of the fault in the mudstone is relatively insignificant. Figure 11b presents the permeability evolution at monitoring points N and M continuously throughout the whole process. The early-stage response illustrates that the initial permeability increase immediately follows the initiation of shear slippage. The permeability at monitoring point N increases sharply to a peak during fracturing; afterward, during the “Hold” and “Extraction” stages, the permeability exhibits a slow but continuous decrease, it indicates that the exploitation would finally reduce the hydraulic conductivity of the fault. However, due to the low initial permeability at monitoring point M, the aggregated pore pressure within the lower fault portion in the conglomerate continues to spread upward and results in the continuous permeability increase during the “Hold” stage, and then it decreases accordingly in the “Extraction” stage.

3.4 Parametric analyses

The prior observations represent the hydromechanical responses of the fault for specific fracturing fluid flow and material properties; these responses define the crucial feedback of stress and fluid pressures on fault slip and permeability evolution. The parametric analyses are carried out by varying a sequence of three conditions while all other conditions remain constant with those of the reference model. Through this analysis, the roles of the (1) fracturing fluid flow rate, (2) initial fault permeability and (3) fault stiffness are separately explored.

The fracturing fluid flow rate is one of the most important factors influencing the evolution of the fault mechanical responses and the permeability features. As the fracturing rate increases, more accumulated pore fluids are able to dissipate along the permeable portion along the fault and even dissipate upward into the low-permeability portion of the fault in the mudstone; the pore pressures increase accordingly. In this case, due to the fault slippage–pressure dependency, the slipped portion of fault is much larger with

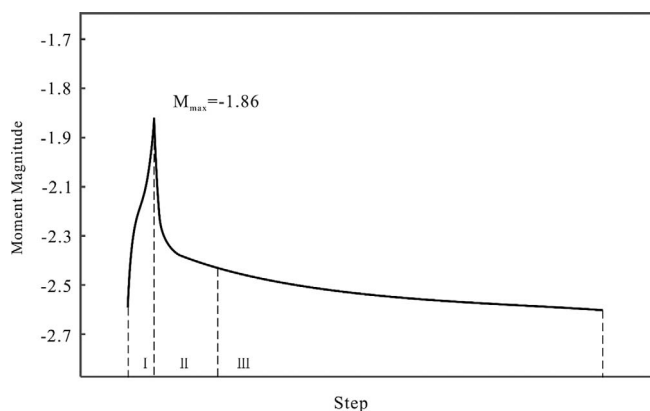


Fig. 10. Moment magnitude Mw evolution of the fault with time.

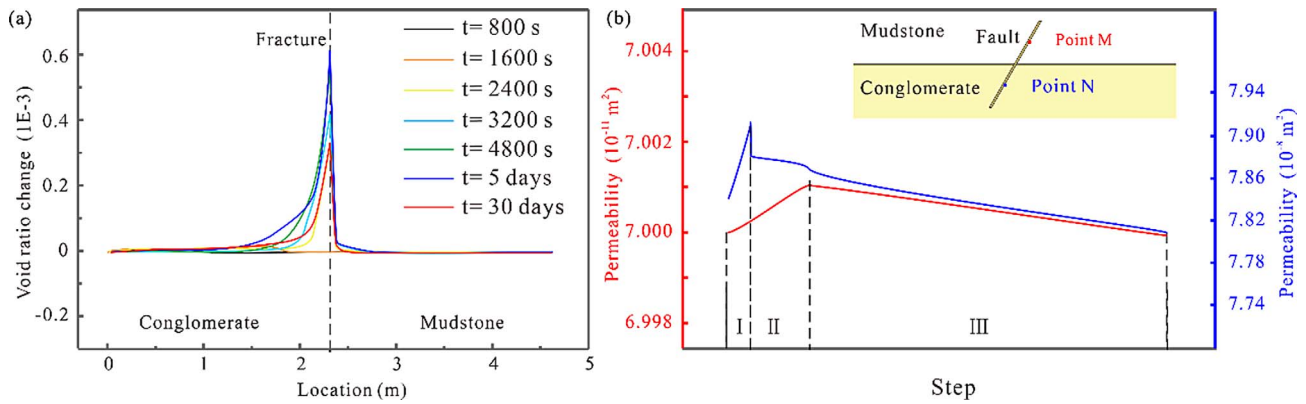


Fig. 11. (a) The void ratio changes along the fault surface at different times and (b) the permeability evolution at monitoring points N and M continuously throughout the whole process.

increasing fracturing fluid flow rate, and the fault portion in the mudstone experiences relatively slight slip (Fig. 12a). The enhanced fracturing fluid flow rate causes the zone of fault slippage concentration to migrate upward. This uniform distribution of fault slippage results in heterogeneous permeability increases along the fault, which consequently change with the fracturing fluid flow rate (Fig. 12b).

To examine the sensitivity of the results to the parameterization of the permeability, we vary the magnitude of the initial permeability of the fault fracture zone from a factor of 1/2 to a factor of 2 with respect to the reference model. When the initial permeability of the fault fracture zones is doubled, since the permeability within these zones is higher than that in the surrounding material, they act as drains connecting the pay zone to the confining formation; the fluid liberated by the enhanced permeability is redistributed hydrostatically; this process dilates the lower portion of the fault, and if the fluid dissipates insufficiently quickly, it leads to permeability change, while the magnitude of the fault slippage remains at the same level (Figs. 12c and 12d). Similarly, we vary the magnitude of the Young's modulus in the fault fracture zone from a factor of 1/2 to a factor of 2 with respect to the reference model. As shown, the reduced Young's modulus redistributes an increasing injection-induced load to the fault and thus decreases both stresses and volumetric compaction within the fault and accordingly reduces the fluid volume available for expulsion through the fault; thus, the decreased pore pressure leads to an insignificant permeability change (Figs. 12e and 12f).

4 Discussion

The analyses discussed in the preceding section examine the role of fault slippage and permeability evolution along the fault surface in connecting the pay zone and the confining formation during the whole process of hydraulic fracturing and production. Early in the evolution, hydrofractures only form near the perforation, and later, they may fully develop and merge with the fault surface. Once they have merged, the tensile stress in front of the hydrofracture tip results

in a concentration of contact stress and shear stress in the vicinity of the fault-fracture intersection, and thus, fault slippage is concentrated there due to the presence of elevated pore pressures generated by the hydrofracturing operation. Further slippage spreads from the zone of high permeability to shallower levels; consequently, the slippages concentrate in the high-permeability fault portion in the conglomerate rather than in the mudstone. The role of the static elastic stress perturbation and the effect of pre-existing faults in the rock volume are consistent with the work of Roche *et al.* (2018) in isotropic formation. The fault experiences the strongest pore pressure migration and induced fault slippage in the “Pump” stage, and afterward, the slip velocity decreases gradually to zero by the end of extraction; thus, the fault slippage finally reaches stabilization.

When the permeability evolves with fault slippage, the upward migration of the permeability-enhanced zone enables the capped pore water within the high-permeability fault portion in the conglomerate to diffuse into the surrounding formation, and even promotes upward migration of the fracturing fluid into the low-permeability fault portion in the mudstone, which increases the risk of fracturing fluid leakage. As a mechanism for the escape of high pore pressures that cannot be accommodated, the permeability evolution is formed naturally as a result of both fault slippage generated by excess pore pressures within the fault and stress disturbance caused by hydraulic fracturing. The permeability-enhanced zone is concentrated at the fracture-fault intersection and mainly localized in the high-permeability fault portion in the conglomerate, and the extent of this zone depends on the magnitude of the fault slippage. However, due to the limited fault slippage and lower initial permeability, the change in conductivity within the upper portion of the fault in the mudstone is relatively insignificant.

Mazzoldi *et al.* (2012) use geological observations and seismological theories to estimate the magnitude of seismic events generated by geological carbon sequestration, the fault is assumed to be circular with radius of 500 m, and the average displacement across the fault surface during a single event is 0.1 m, and the calculated maximum

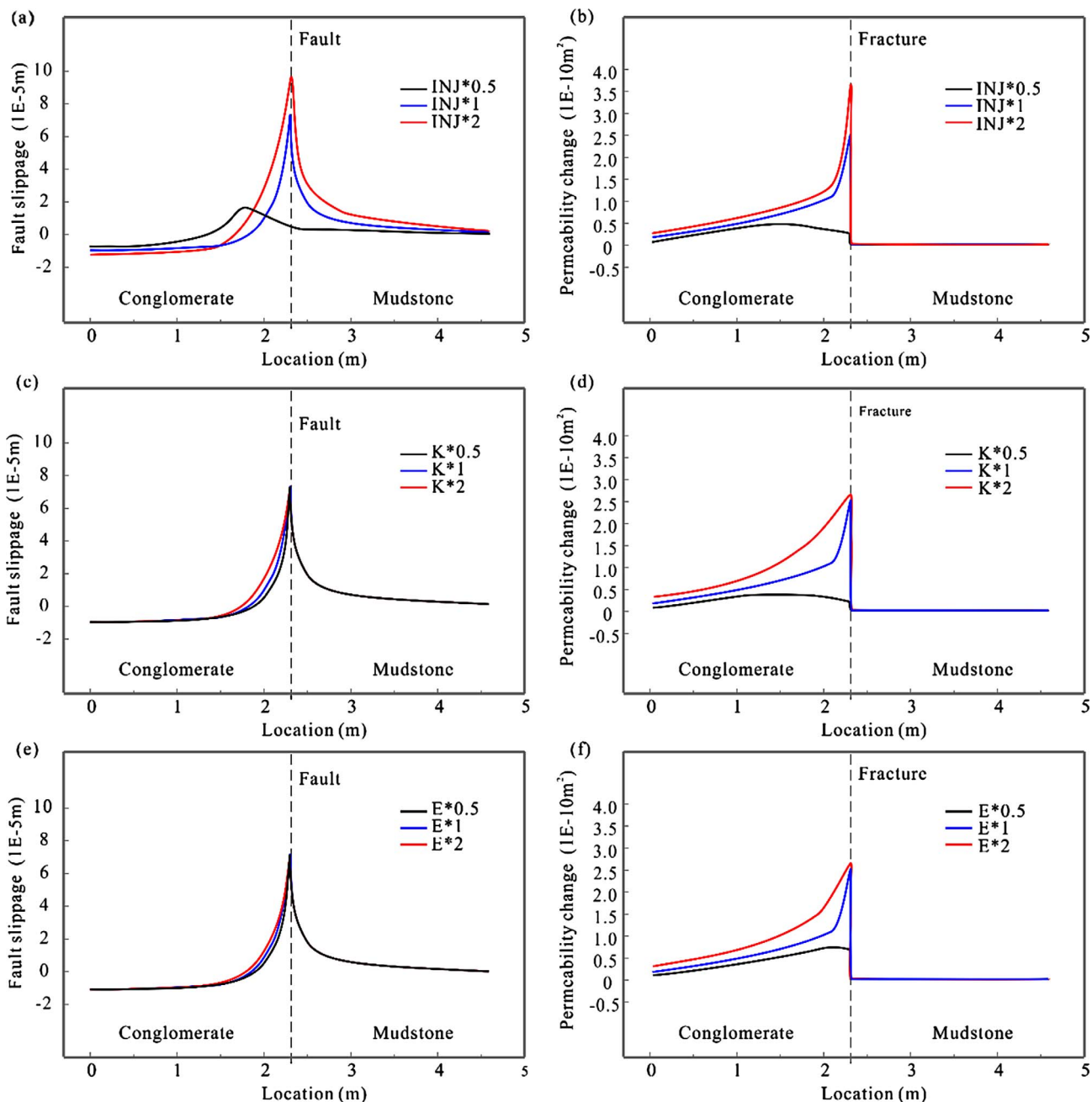


Fig. 12. Fault slippage and permeability contours at 80 min for parametric studies: (a, b) fracturing fluid flow rate, (c, d) initial fault permeability and (e, f) fault stiffness.

magnitude of a seismic event is 3.9. In this work, as the size of undetected fault is limited, the magnitude of a seismic event is significantly reduced. Moreover, the results of parametric analyses indicate that the enhanced fracturing fluid flow rate increases the magnitude and slipped portion of the fault, that the enhanced fracturing fluid flow rate causes the zone of fault slippage concentration to migrate upward and finally to near the fault-fracture intersection, and that the uniform distribution of fault slippage results in accordingly heterogeneous permeability increases along

the fault. In addition, the permeability change of the fault portion in the pay zone is positive relative to the initial permeability and fault stiffness, while the fault slippage remains at the same level. Consequently, even though the hydraulic fracturing operation enhances the vertical conductivity of the pay zone by increasing the permeability of its integral fault, due to the insignificant permeability change of the fault portion within the mudstone, the vertical conductivity of the confining formation is almost unchanged.

5 Conclusion

The conceptual modeling of the fault hydromechanical responses to the whole process of hydraulic fracturing and production accommodates only a limited suite of features. It does not take into account irregular boundary conditions, geothermal transfer or fracturing fluid compression/expansion. However, even without these behaviors, our model is able to show that the fault slippage and permeability evolution are principally controlled by the initial permeability distribution and the fracturing fluid injected into the fault. The main conclusions from the obtained results were summarized as follows:

1. The initial hydrofracture formed at the perforation and propagated upward, once it merged with the fault surface, the existence of an undetected small fault would effectively constrain the hydraulic fracture height evolution.
2. The tensile stress in front of the hydrofracture tip resulted in a concentration of fault slippage at the fracture-fault intersection; the permeability-enhanced zone was also concentrated there and mainly localized on the high-permeability fault portion in the pay zone.
3. As fracturing continued, further slippage spread from the permeability increase zone of high permeability to shallower levels, and the extent of this zone was dependent on the magnitude of the fault slippage. At the end of extraction, the slip velocity decreases gradually to zero by the end of extraction; thus, the fault slippage finally reaches stabilization.
4. The existence of an undetected small fault would effectively constrain the hydraulic fracture height evolution, that the induced microseismic events generally range between $M_w = -1.8$ and -2.6 and that the largest events occur within the “Pump” stage.
5. In the confining formation, the insignificant permeability change does not affect its vertical conductivity in the short term, and then the pore pressure decreases with fluid extraction.

Undetected small faults in Chang 7 member of the *Yanchang Formation* are not capable of generating sufficiently large events that could be felt on the surface, and they may not be the source of large earthquakes. The induced microseismic events could be considered as the sources of acoustic emission events detected while monitoring the fracturing fluid front. Due to the limited fault slippage and lower initial permeability, the CO₂ fracturing operation near undetected small faults could not conduct preferential pathway for upward CO₂ leakage or contaminate overlying shallower potable aquifers.

Acknowledgments. We acknowledge the funding supported by National Natural Science Foundation of China (Grant No. 51809220), Young Scholars Development Fund of Southwest Petroleum University (Grant No. 201699010097), Open Research Fund of State Key Laboratory of Geomechanics and Geotechnical Engineering (Grant No. Z017008).

References

- Abercrombie R.E. (1995) Earthquake source scaling relationships from -1 to 5 ML using seismograms recorded at 2.5-km depth, *J. Geophys. Res. Atmos.* **1002**, 24015–24036.
- Akulich A.V., Zvyagin A.V. (2008) Interaction between hydraulic and natural fractures, *Fluid Dyn.* **43**, 428–435.
- Billi A., Salvini F., Storti F. (2003) The damage zone-fault core transition in carbonate rocks: implications for fault growth, structure and permeability, *J. Struct. Geol.* **25**, 1779–1794.
- Bloch S., Helmold K.P. (1995) Approaches to predicting reservoir quality in sandstones, *AAPG Bull.* **79**, 1, 97–115.
- Brenner S.L., Gudmundsson A. (2004) Arrest and aperture variation of hydrofractures in layered reservoirs, *Geol. Soc. Lond. Spec. Publ.* **231**, 117–128.
- Chapelle S.L., Milsch H., Castelnaud O., Duval P. (1999) Compressive creep of ice containing a liquid intergranular phase: Rate-controlling processes in the dislocation creep regime, *Geophys. Res. Lett.* **26**, 251–254.
- Childs C., Watterson J., Walsh J.J. (1996) A model for the structure and development of fault zones, *J. Geol. Soc.* **153**, 337–340.
- Chong Z., Li X., Chen X. (2017) Effect of injection site on fault activation and seismicity during hydraulic fracturing, *Energies* **10**, 1619.
- Cleary M.P. (1978) Primary factors governing hydraulic fractures in heterogeneous stratified porous formations. *ASME Energy Technical Conference and Exhibition*, 5th November, Houston, TX.
- Dahi-Taleghani A., Olson J.E. (2011) Numerical modeling of multi-stranded hydraulic fracture propagation: Accounting for the interaction between induced and natural fractures, *SPE J.* **16**, 575–581.
- Davies R., Foulger G., Bindley A., Styles P. (2013) Induced seismicity and hydraulic fracturing for the recovery of hydrocarbons, *Mar. Pet. Geol.* **45**, 171–185.
- Dong C.Y., Pater C.J.D. (2001) Numerical implementation of displacement discontinuity method and its application in hydraulic fracturing, *Comput. Methods Appl. Mech. Eng.* **191**, 745–760.
- Dyskin A.V., Caballero A. (2009) Orthogonal crack approaching an interface, *Eng. Fract. Mech.* **76**, 2476–2485.
- Ellsworth W.L. (2013) Injection-induced earthquakes, *Science* **341**, 142.
- Figueiredo B., Tsang C.F., Rutqvist J., Bensabat J., Niemi A. (2015) Coupled hydro-mechanical processes and fault reactivation induced by CO₂ Injection in a three-layer storage formation, *Int. J. Greenhouse Gas Control* **39**, 432–448.
- Figueiredo B., Tsang C.F., Rutqvist J., Niemi A. (2017) Study of hydraulic fracturing processes in shale formations with complex geological settings, *J. Pet. Sci. Eng.* **152**, 361–374.
- Fiori A., Indelman P., Dagan G. (1998) Correlation structure of flow variables for steady flow toward a well with application to highly anisotropic heterogeneous formations, *Water Resour. Res.* **34**, 4, 699–708.
- He M.Y., Hutchinson J.W. (1989) Crack deflection at an interface between dissimilar elastic materials, *Int. J. Solids Struct.* **25**, 1053–1067.
- Hubbert M.K., Willis D.G.W. (1957) Mechanics of hydraulic fracturing, *Dev. Pet. Sci.* **210**, 369–390.
- Ilieva P., Kilzer A., Weidner E. (2016) Measurement of solubility, viscosity, density and interfacial tension of the

- systems tristearin and CO₂ and rapeseed oil and CO₂, *J. Supercrit. Fluids* **117**, 40–49.
- Ishida T., Aoyagi K., Niwa T., Chen Y., Murata S., Chen Q., Nakayama Y. (2012) Acoustic emission monitoring of hydraulic fracturing laboratory experiment with supercritical and liquid CO₂, *Geophys. Res. Lett.* **39**, 16, 1–6.
- Jeanne P., Guglielmi Y., Cappa F., Rinaldi A.P., Rutqvist J. (2014) The effects of lateral property variations on fault-zone reactivation by fluid pressurization: Application to CO₂ pressurization effects within major and undetected fault zones, *J. Struct. Geol.* **62**, 97–108.
- Jia L. (2000) Debonding of the interface as “crack arrestor”, *Int. J. Fract.* **105**, 57–79.
- Kanamori H., Anderson D.L. (1975) Theoretical basis of some empirical relations in seismology, *Bull. Seismol. Soc. Am.* **65**, 1073–1095.
- Khoei A.R., Vahab M., Hirmand M. (2016) Modeling the interaction between fluid-driven fracture and natural fault using an enriched-FEM technique, *Int. J. Fract.* **197**, 1–24.
- Mazzoldi A., Rinaldi A.P., Borgia A., Rutqvist J. (2012) Induced seismicity within geological carbon sequestration projects: Maximum earthquake magnitude and leakage potential from undetected faults, *Int. J. Greenhouse Gas Control* **10**, 434–442.
- Montgomery C.T., Smith M.B. (2010) Hydraulic fracturing: History of an enduring technology, *J. Pet. Technol.* **62**, 26–32.
- Mukuhira Y., Moriya H., Ito T., Asanuma H., Häring M. (2017) Pore pressure migration during hydraulic stimulation due to permeability enhancement by low-pressure subcritical fracture slip, *Geophys. Res. Lett.* **44**, 7.
- Othmani Y., Delannay L., Doghri I. (2011) Equivalent inclusion solution adapted to particle debonding with a non-linear cohesive law, *Int. J. Solids Struct.* **48**, 3326–3335.
- Rinaldi A.P., Rutqvist J., Cappa F. (2014) Geomechanical effects on CO₂ leakage through fault zones during large-scale underground injection, *Int. J. Greenhouse Gas Control* **20**, 117–131.
- Roche V., van der Baan M. (2015) The role of lithological layering and pore pressure on fluid-induced microseismicity, *J. Geophys. Res. Solid Earth* **120**, 2, 923–943.
- Roche V., van der Baan M., Preisig G. (2018) A study of 3D modeling of hydraulic fracturing and stress perturbations during fluid injection, *J. Pet. Sci. Eng.* **170**, 829–843.
- Rutqvist J., Rinaldi A.P., Cappa F., Moridis G.J. (2013) Modeling of fault reactivation and induced seismicity during hydraulic fracturing of shale-gas reservoirs, *J. Pet. Sci. Eng.* **107**, 31–44.
- Savalli L., Engelder T. (2005) Mechanisms controlling rupture shape during subcritical growth of joints in layered rocks, *Geol. Soc. Am. Bull.* **117**, 436–449.
- Smith M.B., Bale A.B., Britt L.K., Klein H.H., Siebrits E., Dang X. (2001) Layered modulus effects on fracture propagation, proppant placement, and fracture modeling, in: *SPE Annual Technical Conference and Exhibition*, 30 September–3 October, New Orleans, LA.
- Swartz T. (2011) Hydraulic fracturing: Risks and risk management, *Nat. Res. Environ.* **26**, 30–59.
- Thomas V.L., Kitanidis P.K. (1989) A numerical spectral approach for the derivation of piezometric head covariance functions, *Water Resour. Res.* **25**, 11, 2287–2298.
- Vengosh A., Jackson R.B., Warner N., Darrah T.H., Kondash A. (2014) A critical review of the risks to water resources from unconventional shale gas development and hydraulic fracturing in the United States, *Environ. Sci. Technol.* **48**, 8334–8348.
- Warpinski N.R., Schmidt R., Northrop D. (1982) In-situ stresses: the predominant influence on hydraulic fracture containment, *J. Pet. Technol.* **34**, 653–664.
- Wei X., Li Q., Li X., Sun Y. (2016) Impact indicators for caprock integrity and induced seismicity in CO₂ geosequestration: Insights from uncertainty analyses, *Nat. Haz.* **81**, 1–21.
- Wei X.C., Li Q., Li X.Y., Sun Y.K., Liu X.H. (2015) Uncertainty analysis of impact indicators for the integrity of combined caprock during CO₂ geosequestration, *Eng. Geol.* **196**, 37–46.
- Zhou J., Chen M., Jin Y., Zhang G.Q. (2008) Analysis of fracture propagation behavior and fracture geometry using a tri-axial fracturing system in naturally fractured reservoirs, *Int. J. Rock Mech. Min. Sci.* **45**, 1143–1152.
- Zoback M.D., Kohli A.H., Das I., McClure M.W. (2012) The importance of slow slip on faults during hydraulic fracturing stimulation of shale gas reservoirs. in: *SPE Americas Unconventional Resources Conference*, 5–7 June, Pittsburgh, PA, USA. Society of Petroleum Engineers.